Geocooling with integrated PCM thermal energy storage in a Mediterranean climate.

Authors:

P. McKenna [a]; W.J.N. Turner [b]; D. P. Finn [a, b]

[a] School of Mechanical and Materials Engineering, University College Dublin (UCD), Belfield, Dublin 4, Ireland.

[b] Energy Institute, University College Dublin (UCD), Belfield, Dublin 4, Ireland.

Keywords:

Geocooling
Phase Change Material (PCM)
Thermal Energy Storage (TES)
Storage Tank
Renewable Energy
HVAC.

Abstract

Geocooling and thermal energy storage (TES) are two strategies that could help alleviate the energy and carbon emission burden from cooling commercial buildings. This simulation study analyses the potential for geocooling, both with and without TES, in a Mediterranean climate. Spherically-encapsulated phase change material (PCM) was used as the thermal storage medium in the TES system. A new, advanced PCM TES tank model was developed and validated within the TRNSYS environment. Using a small, lightweight commercial building as a case study, it was found that electricity savings of between 24 and 45% are possible from combining geocooling with TES, when compared to a system based on a reference ground-source heat pump (GSHP).

1. Introduction

This paper explores the potential for using geocooling or 'geothermal free cooling' in combination with thermal energy storage (TES) to reduce the energy and carbon impact of cooling a small, lightweight commercial building located in a Mediterranean climate [1,2]. Validated computer simulation models are developed and then used to assess the energy performance of the two technologies, both independently and co-dependently.

Buildings account for approximately 30 to 40% of total primary worldwide energy consumption. This figure is growing with population increase and also as thermal comfort becomes more of a necessity than a luxury [3]. In terms of electricity consumption, the proportion attributed to buildings is even higher. In OECD (Organisation for Economic Co-operation and Development) countries, approximately 55% of all electricity generated is consumed in residential and commercial buildings, while in Europe this value is 44% [4]. In commercial buildings, Pérez-Lombard *et al.* [3] state that heating, ventilation and air conditioning (HVAC) systems use close to 50% of the total energy consumed, while Roth *et al.* [5] put this figure at 30%. Due to the high quantity of energy used in HVAC systems worldwide, even small increases in system efficiency can lead to substantial energy savings.

Two technologies that offer potential to increase building energy efficiency are geocooling and thermal energy storage (TES). Geocooling exploits the near-constant annual temperature of the ground [6]. During the warmer seasons, the ground temperature in Mediterranean climates is lower than the ambient air temperature. This temperature difference can be exploited using a borehole heat exchanger and a heat transfer fluid (HTF) to provide cooling to building HVAC systems. This 'free' cooling can be used to offset the electricity consumption of air conditioners and reduce overall building energy consumption [7].

TES is a technology that decouples the thermal energy demand of a building from peak ambient weather temperatures. A TES system can be charged at night, when the demand for electricity and its cost are lowest, and then discharged through the building HVAC system during the day, when the demand for thermal conditioning is highest. This 'load shifting' is a form of demand-side management (DSM), and a crucial pathway to optimising the power system of many countries and reducing their carbon emissions [8].

Price [9] states that energy efficient operation of an HVAC system is building specific; therefore, a building with phase change material (PCM) TES, GSHP and geocooling bypass was chosen as the focal point of this research. The aim of the research is to examine an integrated GSHP system with geocooling and PCM TES with emphasis on the effect of the operational strategy on the overall system performance. To meet this aim, a detailed, verified, TRNSYS mathematical model of the integrated system is developed.

The novelty of this paper is threefold:

1) To date there have been no studies that analyse the potential of geocooling in commercial buildings in a Mediterranean climate;
2) System-level energy benefits between geocooling and TES applications in commercial buildings have not yet been studied; and
3) A new and advanced mathematical model for a TES tank containing spherically-encapsulated phase change material (PCM) is developed and validated against

experimental data, and then integrated into an HVAC system model containing a ground-source heat pump (GSHP).

The remainder of this paper is organised as thus: in Section 2 the background information required to contextualise this new body of work is described; within Section 3 the development of the PCM TES model and its validation are described; Section 4 explores the use of geocooling and TES in a Mediterranean climate through the simulation of three case-study HVAC systems in a commercial building; Section 5 documents the results from the case study; and finally, in Section 6 conclusions are drawn from the work presented.

2. Background

2.1. Geocooling

Geocooling exploits the temperature difference between the ground, which is near-constant below approximately 10 m (see Figure 1), and the summer-time ambient air. Typically, a ground heat exchanger is used to harness the cooling potential. Water (or some other heat transfer fluid) is chilled while it circulates through horizontal or vertical borehole heat exchangers, and then passed through an air handling unit (AHU), fan coil unit (FCU) or radiant cooling system to supply building cooling [10]. As there is no vapour-compression refrigeration cycle, electricity is only required to drive pumps and fans, which can lead to energy savings over traditional air conditioning systems. Annual system seasonal performance factors (SPFs) of up to 20 have been observed in case studies [10].

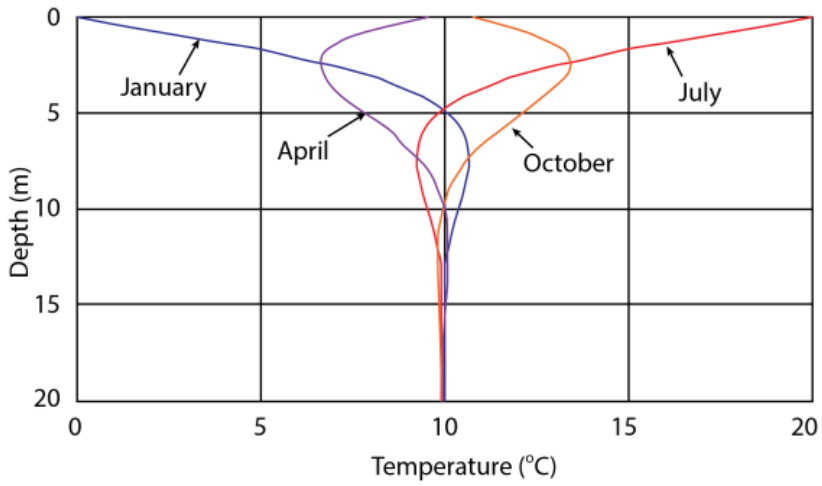

Figure 1: Variation of ground temperature with depth for climatic conditions in Germany [6].

This technology has been shown to be feasible for cool climatic regions [11], as well as for buildings in Switzerland [7] and Germany [6]. An investigation of heat transfer in a ground heat exchanger for different climates indicates that geocooling might be feasible in warmer Mediterranean climates [6]. Lund *et al.* [12] stated that geocooling had been marketed to the residential end-use sector, but little interest has been shown. The use of geocooling is still rare and ground-source heat pumps (GSHPs) are commonly used instead to allow geothermal energy to be harnessed, from the small scale, such as individual domestic residences, up to large-scale district heating and cooling applications [13].

Within the literature, studies on the use of geocooling are sparse. However, three such reports of relevance are presented below.

Eicker and Vorschulze [10] presented two case studies where geocooling was used in German buildings. The first case study considered a building with two rooms: a seminar room where ventilation air was cooled in an AHU, and a foyer with activated concrete floor cooling. The system seasonal performance factor (SPF) was measured to be 20.1 for the first year of operation and 13.5 for the second year. The temperature in the seminar room was maintained below 26°C for the entire season using geocooling. In the foyer, the restricted floor surface area and the low temperature difference between water and room temperatures led to a low maximum cooling power. Within the borehole heat exchanger, a maximum heat transfer rate of about 26 W/m was calculated.

The second case study investigated the use of a horizontal ground heat exchanger for cooling ventilation air [10]. Due to the low proximity and low depth of the heat exchanger tubes, outlet temperatures were about 3°C higher than for the vertical heat exchanger. Consequently, the maximum heat transfer rate in the heat exchanger was approximately 8 W/m. The high outlet temperatures led to insufficient cooling of the ambient air and a larger ground heat exchanger was recommended. Simulations of a ground heat exchanger were also used to examine the potential of geocooling for four different climatic conditions with Madrid being the coldest location and Crete the warmest. For these simulations, the heat transfer in the ground heat exchangers was tabulated with average heat transfer of 20 W/m in Madrid compared to 7.3 W/m in Crete – a significant difference due to the ground conditions. These calculations did not include a building model, and a constant inlet temperature of 22°C to the ground heat exchanger was assumed.

Pahud *et al.* [7] investigated the use of geocooling for a low-energy office building in Switzerland. Cooling was supplied via massive concrete slabs between floors which had plastic pipes embedded in them, through which water flowed from the ground heat exchanger. Internal thermal gains peaked at 26 W/m^2 with average (but low) gains over the year reported as 6 W/m^2. It was calculated that the temperature in the building could be kept below 26.5°C for all but 40 hours of the year. The main contribution of the paper was a method for sizing borehole heat exchangers based on the annual heating-to-cooling ratio and thermal loads of the building.

Wu *et al.* [11] examined the use of geocooling for a cold region in China, where cooling would not normally be employed. Geocooling allowed heat to be added to the ground during the summer to mitigate the thermal degradation of the ground due to a heating-only system. Simulations were performed for buildings located in three cities in northern China. The test building was heated and cooled using an underfloor radiative system with a ground-source absorption heat pump for heating. The effect of using geocooling on the ground temperature and the heating performance of the heat pump was presented. Wu *et al.* found that thermal imbalance in the ground can be effectively eliminated and that heat pump performance was up to 30% higher after a 10-year period.

The aforementioned studies indicate that geocooling may have an application in warmer climates, but to date this has not been tested with either experiments or simulations that include a building or building model and HVAC system. Furthermore, there has been no analysis on the use of geocooling in combination with TES. The current paper looks to address these shortcomings of the current literature by modelling and analysing the performance of an integrated geocooling and TES system in a warm, Mediterranean climate.

2.2. Thermal Energy Storage (TES)

With increased penetration of renewable energy, the variable nature of solar and wind electricity generation leads to the requirement for increased energy storage. Denholm and Hand [14] found that, for a theoretical grid with combined wind and solar electricity generation of up to 80% of demand, in order to limit renewable energy curtailment to 10%, a combination of load shifting and storage equal to about one day of average demand is needed.

The use of thermal energy storage (TES) provides flexibility to the electricity grid which can yield advantages regarding power capacity, generation and curtailment. The U.S. Department of Energy states that energy storage can accelerate the expansion of the grid, and be a "critical component of grid stability and resiliency" [15]. One potential storage solution is distributed TES on the demand side of the grid. The use of distributed thermal energy storage for HVAC systems in buildings "can represent significant value to the energy system" [16] as well as helping to increase the amount of renewables in the energy mix [17].

There are also benefits from TES for building owners. The use of off-peak electricity pricing to produce hot or cold thermal energy during the night time means that on-peak electricity consumption can be reduced, resulting in monetary savings if appropriate pricing tariffs are in place [18].

Phase change material (PCM) is often used in large tanks as a practical implementation of TES. PCM exploits the latent heat of a material undergoing a phase change to store thermal energy. While PCM changes between solid and liquid phases the enthalpy of the PCM increases but the temperature does not.

There have been mathematical models of PCM TES tanks published in the literature [19–25], as well as analyses of control solutions for the deployment of the stored energy [26–29]. Ibáñez et al. [24] developed a model to analyse the deployment of PCM in a domestic hot water tank. Wei et al. [30] studied heat flow in a PCM tank under different capsule properties and geometric configurations. Bellan et al. [31] developed a PCM TES model for integration in a concentrating solar power plant operating at high temperatures (300 to 400°C) using synthetic oil as the heat transfer fluid (HTF) and sodium nitrate as the PCM. Jones and Finn describe the development of an integrated TES and HVAC model for use in heating applications, where the TES PCM system has a transition temperature of 46^{o}C. However, a system-level analysis of PCM TES integrated with a GSHP and a building cooling HVAC application remains absent from the literature until now.

To summarise, this paper addresses three gaps in the literature; namely, the assessment of:

1) The potential for using geocooling in commercial buildings in a Mediterranean climate;
2) System-level energy benefits between geocooling and TES applications in commercial buildings; and
3) System-level performance of PCM TES with an integrated GSHP using a new and advanced mathematical model for a PCM TES tank.

3. PCM Thermal Energy Storage Tank Model

This section describes the PCM TES model and its subsequent validation. The PCM TES tank model will be integrated into a building HVAC and geocooling system model for a case study

outlined in Section 4. The model is based on a cylindrical tank oriented horizontally, with a volume of 0.5 m^3. The length of the tank is 2 m and it has a diameter of 0.6 m. The tank is filled with spherical capsules of 98 mm diameter and 1 mm wall thickness, that are moulded from a blend of polyolefins. The capsules are filled with a 0°C melting-point PCM that consists of water mixed with nucleating agents [32] to minimise sub-cooling [33]. A void fraction (the fraction of the inner volume of the tank taken up by the PCM) of 40% is assumed for the tank [30,34].

3.1. Model Assumptions

The following assumptions were adhered to for the formulation of the PCM TES tank model:

- There is no radial variation of temperature or fluid flow,
- There are no heat losses from the tank,
- The tank is split into N nodes, each of which has homogeneous heat transfer fluid and PCM temperatures,
- All fluid properties are constant with temperature,
- There is no internal heat generation and no radiant heat transfer.

3.2. Model

The PCM tank model is based on the equations for enthalpy and heat transfer in a packed bed developed by Schumann [35]. The enthalpy method is used to represent the phase change process [36]. Schumann's equations can be written in the form:

$$\varepsilon \rho_f c_f \left(\frac{\partial T}{\partial t} + v_\infty \frac{\partial T}{\partial x} \right) = h_p a_p (\Theta - T) - U_w a_w (T - \Theta) \qquad Eq.1$$

for the heat transfer fluid (HTF), and:

$$(1 - \varepsilon) \rho_s c_s \frac{\partial \Theta}{\partial t} = h_p a_p (\Theta - T) \qquad Eq.2$$

for the solid bed, or in this case, PCM capsules.

The left-hand side of Equation 1 represents the heat transfer resulting from a change of temperature of the HTF at the current location, as well as the transfer of heat by convection along the direction of fluid flow. The right-hand side of Equation 1 represents the heat transfer between the PCM and the HTF and the heat loss from the tank (assumed to be zero), respectively.

The left-hand side of Equation 2 represents the change in internal heat of the PCM with time, while the right-hand side represents the heat transfer between the HTF and the PCM, similar to the first term on the right-hand side of Equation 1. These two equations form the basis from which the calculation for the heat transfer from the PCM to the HTF will be determined. This analysis involves the discretisation of the tank into N control volumes, each with length l/N or Δx (Figure 2). Equation 1 is used to calculate the temperature of the HTF leaving a control volume (T_{n+1}) in terms of the inlet temperature of the HTF to the control volume (T_n) and the temperature of the PCM in the control volume (Θ).

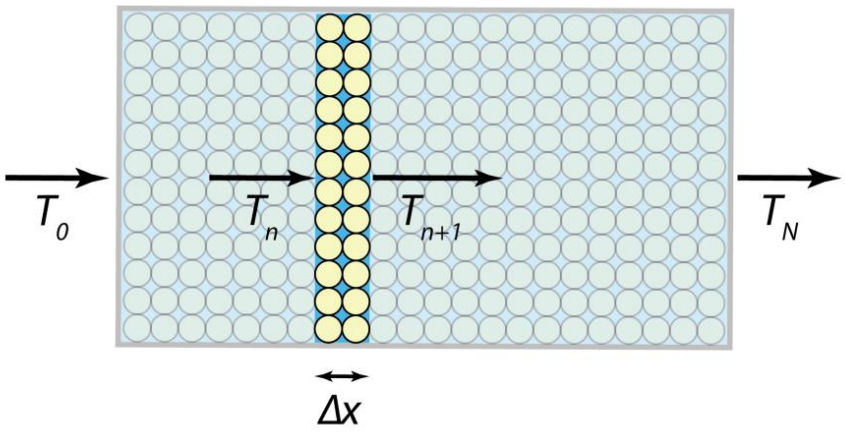

Figure 2: Longitudinal cross-section of the cylindrical PCM thermal storage tank with element of length Δx.

Heat losses from the tank and the rate of change of the fluid temperature with time can be neglected [23], so the heat transfer from the PCM is equal to the heat leaving the control volume via flow of the HTF (Equation 3):

$$\varepsilon \rho_f c_f v_\infty \frac{dT}{dx} = h_p a_p (\Theta - T) \qquad Eq.3$$

Which can be rearranged and then integrated over a control volume, n:

$$\int_n^{n+1} \frac{h_p a_p}{\varepsilon \rho_f c_f v_\infty} dx = \int_n^{n+1} \frac{1}{\Theta - T} dT \qquad Eq.4$$

And then solved to give:

$$\frac{T_{n+1} - T_n}{\Theta - T_n} = 1 - exp\left(\frac{-h_p a_p l}{\varepsilon \rho_f c_f v_\infty N}\right) \qquad Eq.5$$

where l/N is the length of the tank divided by the number of elements being simulated, i.e. the length of one element, Δx. Equation 5 can be rearranged to solve for $T_n + 1$ in terms of T_n and Θ:

$$T_{n+1} = T_n + (\Theta - T_n)\left[1 - exp\left(\frac{-h_p a_p l}{\varepsilon \rho_f c_f v_\infty N}\right)\right] \qquad Eq.6$$

Equation 6 allows the temperature of the fluid leaving an element to be calculated based on the inlet temperature of the fluid to the element and the temperature of the PCM in the element. Equation 6 only includes the convection heat transfer between the capsule wall and the fluid, h_p, which is replaced with $1/A \cdot R_{total}$, where R_{total} is the sum of the thermal resistances to heat transfer (see Figure 3):

$$T_{n+1} = T_n + (\Theta - T_n)\left[1 - exp\left(\frac{-a_p l}{\varepsilon \rho_f c_f v_\infty N \cdot A \cdot R_{total}}\right)\right] \qquad Eq.7$$

The overall thermal resistance, R_{total} is calculated as follows:

$$R_{total} = R_{ext} + R_c + R_{int} \qquad Eq.8$$

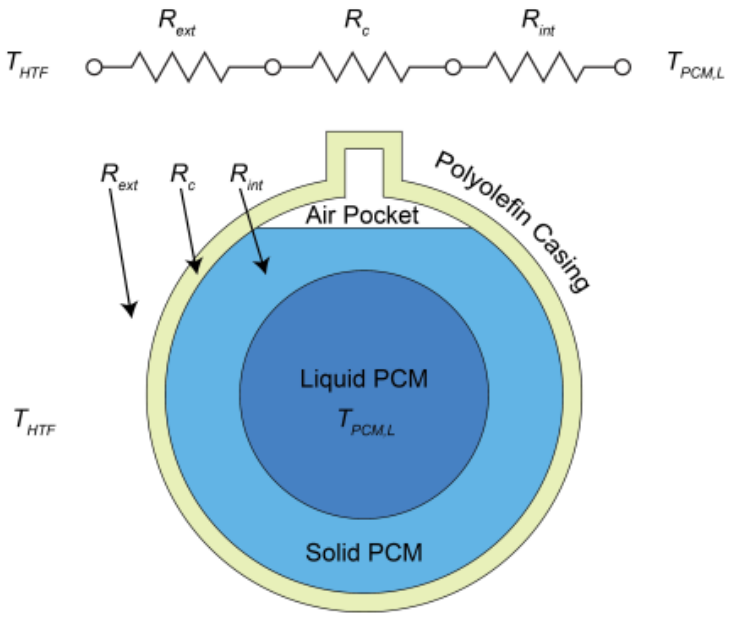

Figure 3: Thermal resistance of a spherical PCM capsule in cooling mode.

R_{int} is neglected during melting as the thermal resistance of a liquid layer is significantly lower than a solid layer due to convection in the liquid. During solidification R_{int} is defined as the thermal resistance for conduction between two concentric spheres. Equation 9 is used to calculate the thermal resistance of the capsule shell, R_c [37]:

$$R_c = \frac{\frac{1}{r_p} - \frac{1}{r_c}}{4\pi k} \qquad Eq.9$$

where r_p is the radius of the PCM, or the inner radius of the capsule wall, and r_c is the outer radius of the capsule wall. The presence of the air pocket is neglected in the model. Equation 9 can also be used to calculate R_{int} by writing the radius of the liquid portion of the PCM, r_{in}, in terms of the liquid fraction of the PCM, X_l, and the outer radius of the PCM, r_p:

$$r_{in} = r_p \sqrt[3]{X_l} \qquad Eq.10$$

$$R_{int} = \frac{1 - \sqrt[3]{X_l}}{4\pi k r_p \sqrt[3]{X_l}} \qquad Eq.11$$

Then R_{ext} can be calculated using the following Nusselt number correlation [23]:

$$N_u = 2 + 1.1[6(1-\varepsilon)]^{0.6} Re_{D_c}^{0.6} Pr_f^{\frac{1}{3}} \qquad Eq.12$$

$$R_{ext} = \frac{D_c}{4k_f A \cdot N_u} \qquad Eq.13$$

Equations 9, 11, and 13 are used to calculate the total thermal resistance to heat transfer between the PCM and the HTF, R_{total}. The outlet temperature from an element is then calculated based on the inlet HTF temperature and the temperature of the PCM (Equation 7). This results in N simultaneous equations from which the temperature of the HTF in every

element can be calculated, once the inlet temperature to the PCM tank is known. Equation 2 is used to calculate the temperature change of the PCM with time. An explicit first-order, finite-difference approximation of this equation yields the following:

$$(1-\varepsilon)\rho_s c_s \frac{\Theta_n^{i+1}-\Theta_n^i}{\Delta t} = h_p a_p \left(T_n^i - \Theta_n^i\right) \qquad Eq.14$$

To enable the use of the enthalpy method to represent the phase change process, the temperature change of the PCM over time is represented as a change in specific enthalpy, H, leading to Equation 15:

$$H_n^{i+1} = H_n^i + \frac{a_p \Delta t}{(1-\varepsilon)\rho_s A \cdot R_{total}} \left(T_n^i - \Theta_n^i\right) \qquad Eq.15$$

From Equation 15 the change in enthalpy of the PCM for the next time-step can be calculated. To calculate the temperature of the PCM, the melting point of the PCM is assumed to occur over a finite temperature range, $T_{m,l}$ to $T_{m,h}$. The latent heat of fusion is spread linearly over this temperature range. It is also assumed that the specific heats of the solid and liquid PCM are constant.

The temperature-enthalpy relation of the PCM is split into three distinct phases:

PCM fully solid:	$H = c_{p,s}\Theta;$	$\Theta < T_{m,l}$	$Eq.16$
PCM melting/freezing:	$H = c_{p,s}T_{m,l} + \frac{L}{T_{m,h}-T_{m,l}}\left(\Theta - T_{m,l}\right);$	$T_{m,l} < \Theta < T_{m,h}$	$Eq.17$
PCM liquid:	$H = c_{p,s}T_{m,l} + L + c_{p,l}\left(\Theta - T_{m,h}\right);$	$\Theta > T_{m,h}$	$Eq.18$

Equations 16, 17 and 18 are used to calculate the PCM specific enthalpy if the PCM temperature is known and vice versa.

To accurately model sub-cooling of the PCM, different values of $T_{m,l}$ and $T_{m,s}$ were selected for heating and cooling. The values were chosen as part of the validation procedure to ensure an accurate fit with experimental results. Values selected were $T_{m,l} = -2.0°C$ and $T_{m,s} = -2.8°C$ for cooling; and $T_{m,l} = 3.0°C$ and $T_{m,s} = 0.0°C$ for heating. The different melting ranges approximate the apparent hysteresis associated with PCM phase change [38]. There is a potential source of inaccuracy due to the use of the assumption by Regin *et al.* [23] that the rate of change of fluid temperature with time is negligible. Any changes in inlet temperature propagate through the tank within one time step because the model as described above uses the outlet temperature from a node as the inlet temperature for the next node in the same time step. This approach disregards the time taken for the HTF to flow through the tank. To rectify this modelling issue, the number of nodes is calculated so that the distance that the HTF travels in one time step is equal to the length of one node. The outlet temperature from a node is then set as the inlet temperature to the next node for the next time step. This mechanism is shown in Figure 4, where the dashed lines represent the progression of the HTF as modelled by Regin *et al.* [23]. It can be seen that the inlet temperature of the HTF at time step i will affect the HTF temperature at all of the nodes, but will have no effect on the HTF temperatures at the next time step, $i+1$. The modified solution, shown as a solid line in Figure 4, is a more realistic representation of the HTF as it flows through the tank. In this solution, the outlet temperature for node n at time i becomes the inlet temperature for node $n+1$ at time step $i+1$.

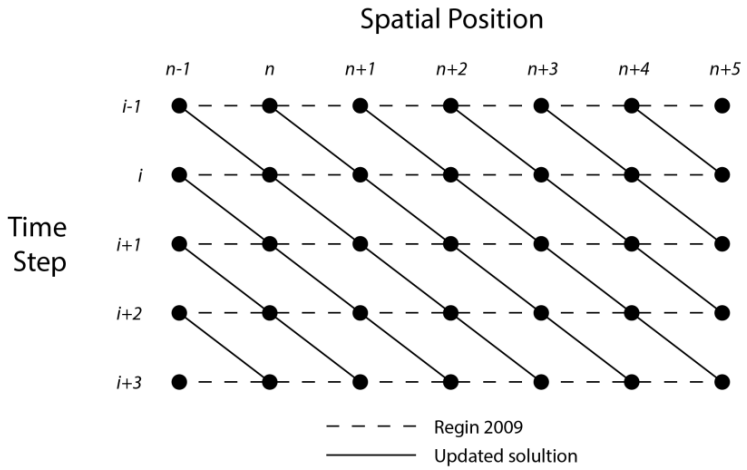

Figure 4: Progression of HTF temperature calculation in space and time.

3.3. Validation

Validation used experimental data from Bédécarrats *et al.* [19], who analysed a PCM TES tank with very similar properties to the modelled tank (see Table A1 in the Appendix). Simulations were performed within the TRNSYS environment [39], recreating the experimental conditions. Sixteen validation simulations were conducted; eight for tank charging (see Table 1) and eight for tank discharging (see Table 2).

Simulation duration was 20 h with a time step of 1 s. The time period of 20 h is approximately equal to the longest experimental charging time of the PCM tank. The initial temperature of the HTF and the PCM were assumed to be homogenous for all nodes at the beginning of each simulation. The experimental and modelled PCM has the same melting temperature and both were encapsulated in spheres of a comparable diameter (77 mm and 98 mm). The HTF for both was a mixture of glycol and water.

The root-mean-square error (RMSE) and mean absolute percentage error (MAPE) were used as performance metrics to quantify the model performance:

$$RMSE = \sqrt{\frac{1}{n}\sum_{i=1}^{n}\left(T_i - \hat{T}_i\right)^2} \qquad Eq.19$$

$$MAPE = \frac{1}{n}\sum_{i=1}^{n}\left|\frac{T_i - \hat{T}_i}{\hat{T}_i}\right| \qquad Eq.20$$

Where, T_i is the simulated temperature, and $\hat{T}_i$ is the experimental temperature at time step i, and n is the total number of time steps. Degrees Kelvin is used for the MAPE calculations.

Thermal Charging

Table 1 shows the results for validation of the PCM tank thermal charging. There are eight different flow rate/inlet temperature combinations. The HTF flow rates ($\dot{V}$) range from 1.1 m^3/h to 2.5 m^3/h, while the tank inlet temperatures range from -3.8°C to -6.1°C. These combinations can be seen in Table 1. The tank inlet temperature is not a constant value, but begins at the initial temperature of the tank, T_{init}, and decreases at the rate of 4°C/h until it reaches T_{in}.

All of the simulations show good agreement with the experimental results. The RMSE varies between 0.17 and 0.52°C. The MAPE varies between 0.06 and 0.15%.

Table 1: Simulation parameters and results for the PCM tank thermal charging validation.

Experiment No.	$\dot{V}$ (m^3/h)	T_{init} (°C)	T_{in} (°C)	RMSE (°C)	MAPE (%)
1	1.3	6.30	-6.10	0.50	0.15
2	2.4	6.30	-3.80	0.20	0.07
3	2.4	6.30	-5.00	0.17	0.06
4	2.4	6.30	-6.10	0.18	0.06
5	1.1	6.30	-6.10	0.52	0.14
6	1.5	6.30	-6.10	0.43	0.13
7	2.0	6.30	-6.10	0.23	0.07
8	2.5	6.30	-6.10	0.17	0.06

Plots of the experimental and simulated HTF outlet temperature are shown in Figure 5, where the red line is a plot of the simulated outlet temperature while the blue line indicates the experimental measurements. The instantaneous error is plotted in green and the RMSE and MAPE for the whole simulation is displayed on each graph.

In Figure 5, the highest instantaneous errors tend to be at the beginning of the simulation where the HTF inlet temperature is changing. This portion of the simulation has the largest variation in temperatures and the higher errors seen may be due to these more rapidly changing temperatures. Although the highest errors were observed at the initial part of the simulation, in Figure 5a (Experiment 1) there are errors approaching 1°C towards the end of the simulation. These errors are significantly higher than those observed at a similar point in the other simulations and lead to a large error in total charging time of 2.0 h. The other simulations demonstrate a total charging time closer to the experimental results. Although there are portions of the simulations with relatively high errors, these error values were low enough that the overall accuracy of the model was not significantly affected and a highest RMSE of 0.52°C can be deemed as acceptable for the model [40].

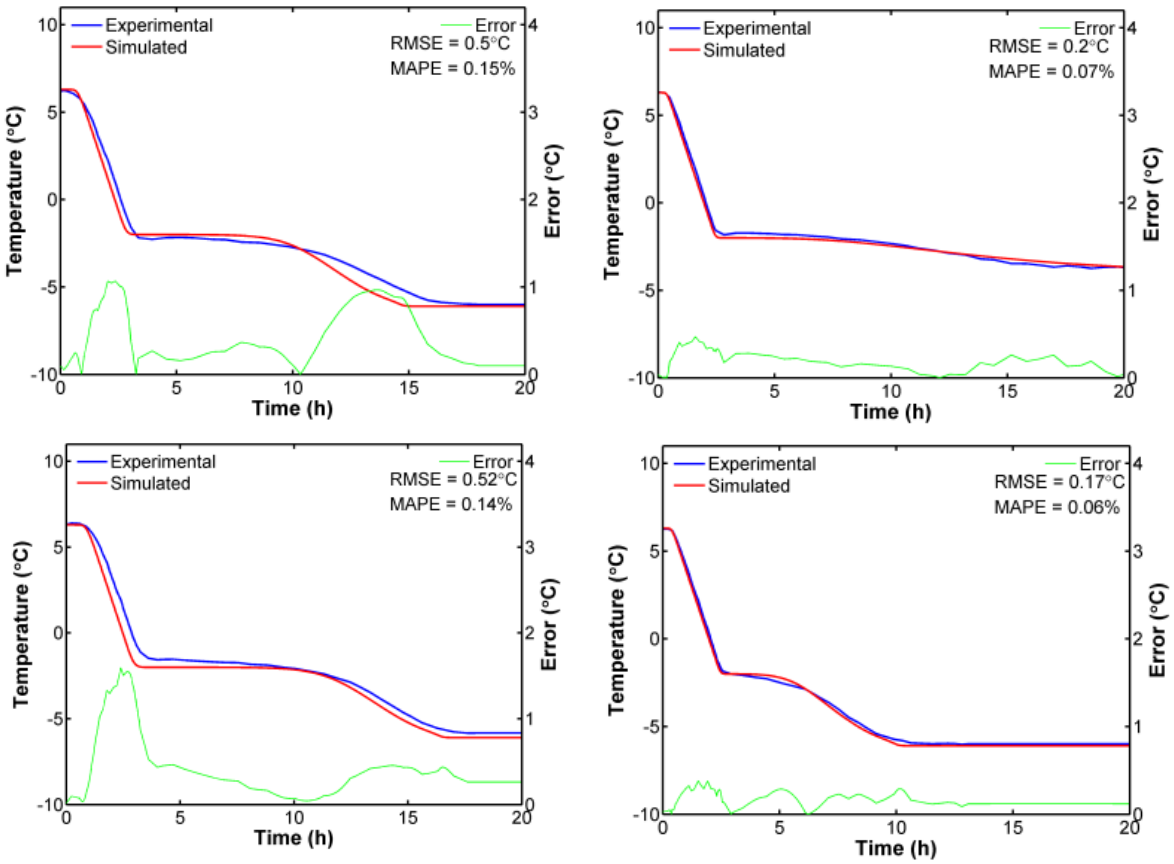

Figure 5: PCM tank thermal charging validation for (clockwise from top-left) Experiments 1, 2, 5 and 8. Experimental data from Bédécarrats et al. [19].

Figure 6 shows the heat transfer rate to the PCM, the temperature of the PCM and the solid fraction of the PCM for different cooling powers. (i.e., the cooling power used to remove thermal energy from the PCM).

The charging characteristics of the tank for four different heat transfer rates are shown in Figure 6. The charging ceases if the outlet temperature from the tank, T_{out}, falls below -15ºC. The HTF volume flow rate is 1.5 m^3/h and the cooling power supplied to the HTF, $\dot{Q}_{HTF}$ is shown at 2, 4, 8 and 15 kW, respectively, for Figure 6a to 6d.

As the cooling rate supplied to the HTF increases, the time taken for the tank to charge decreases. The total charging time for 2 kW of cooling is almost double that for 4 kW, at 14 h and 7.1 h respectively. As the charging power increases to 8 kW and 15 kW, the time for complete charging of the tank drops to 3.8 h and 2.3 h respectively. The solid fraction of PCM, X_S, is also shown in Figure 6. The solid fraction increases to 1.0 as the TES tank is cooled and the PCM freezes.

The total cooling energy stored in the tank depends on the temperature of the PCM, but for each of the four charging conditions the tank holds approximately 26.5 kWh.

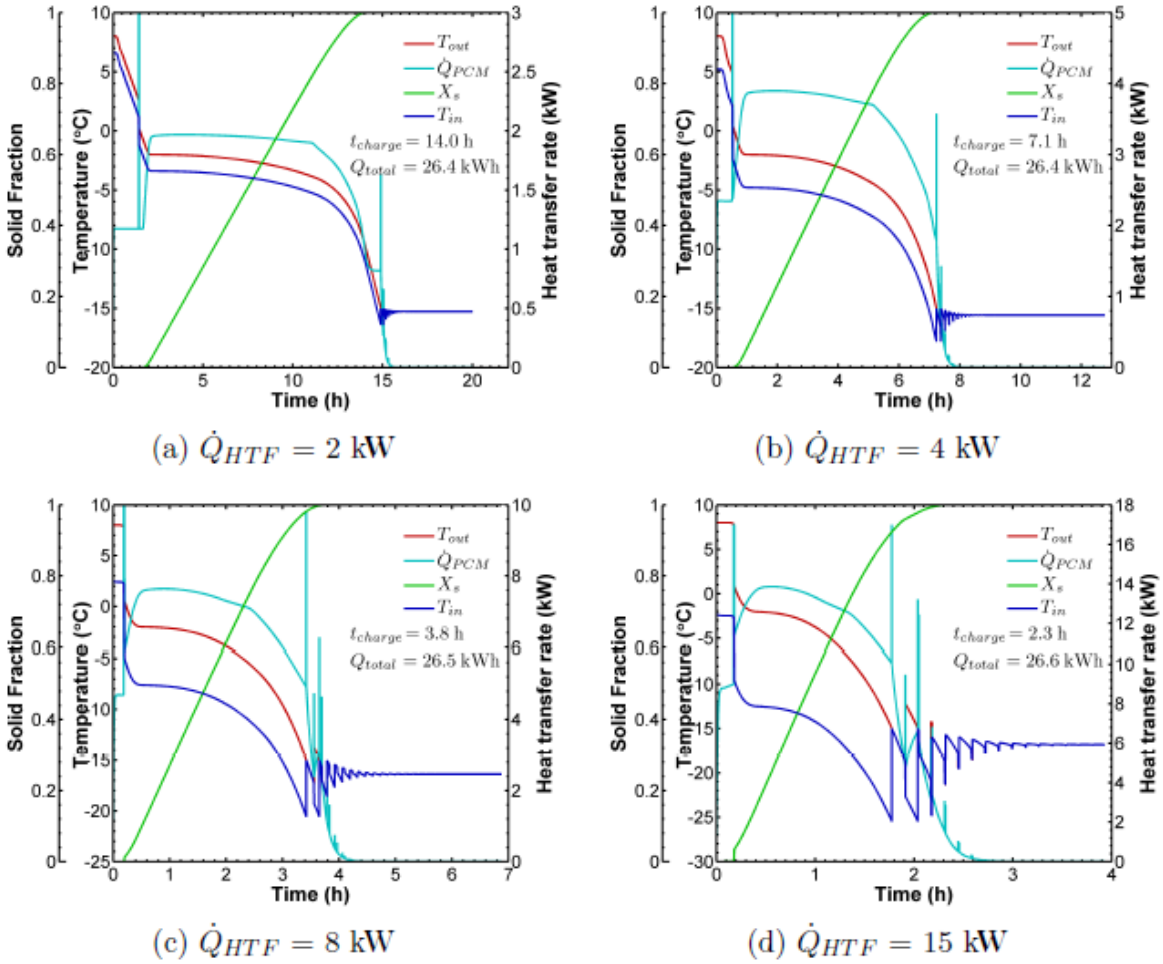

(a) $\dot{Q}_{HTF} = 2$ kW (b) $\dot{Q}_{HTF} = 4$ kW

(c) $\dot{Q}_{HTF} = 8$ kW (d) $\dot{Q}_{HTF} = 15$ kW

Figure 6: Properties under charging, for varying cooling power supplied to the TES tank.

Thermal Discharging

Table 2 shows the thermal discharging results for validation of the PCM tank model. In this case, $\dot{V}$ ranges from 1.0 m^3/h to 2.3 m^3/h, while the inlet temperatures range from 5.1°C to 10.3°C. Again, the inlet temperature begins at T_{init} and increases until it is equal to T_{in}. For discharging the temperature increases at 10°C /h compared to 4°C /h for charging.

Table 2: Simulation parameters and results for the PCM tank thermal discharging validation.

Experiment No.	$\dot{V}$ (m^3/h)	T_{init} (°C)	T_{in} (°C)	RMSE (°C)	MAPE (%)
9	1.1	-5.50	5.50	0.30	0.04
10	1.0	-6.20	6.20	0.33	0.07
11	1.5	-6.20	6.20	0.29	0.07
12	2.0	-6.20	6.20	0.28	0.06
13	2.3	-6.20	6.20	0.28	0.07
14	1.0	-7.60	5.10	0.39	0.09
15	1.0	-6.10	7.10	0.44	0.07
16	1.0	-5.00	10.30	0.57	0.11

Similar to the charging validation, individual plots of the experimental and simulated HTF outlet temperature are shown in Figure 7. The errors for discharging the PCM tank are comparable to those for charging. The RMSE for the individual simulations ranges from 0.28°C

to 0.57°C, which is slightly higher than the errors for charging, while the MAPE varying from 0.04% to 0.11%, which is slightly lower. Although the average error results are similar, the maximum instantaneous errors are higher, with errors as high as 3.2° in Experiment 14. This error was at the beginning of the simulation, where the inlet temperature to the tank is decreasing. This portion of the simulation shows the highest errors for all of the simulations. The errors may be amplified in this case due to the higher rate of change of inlet temperature.

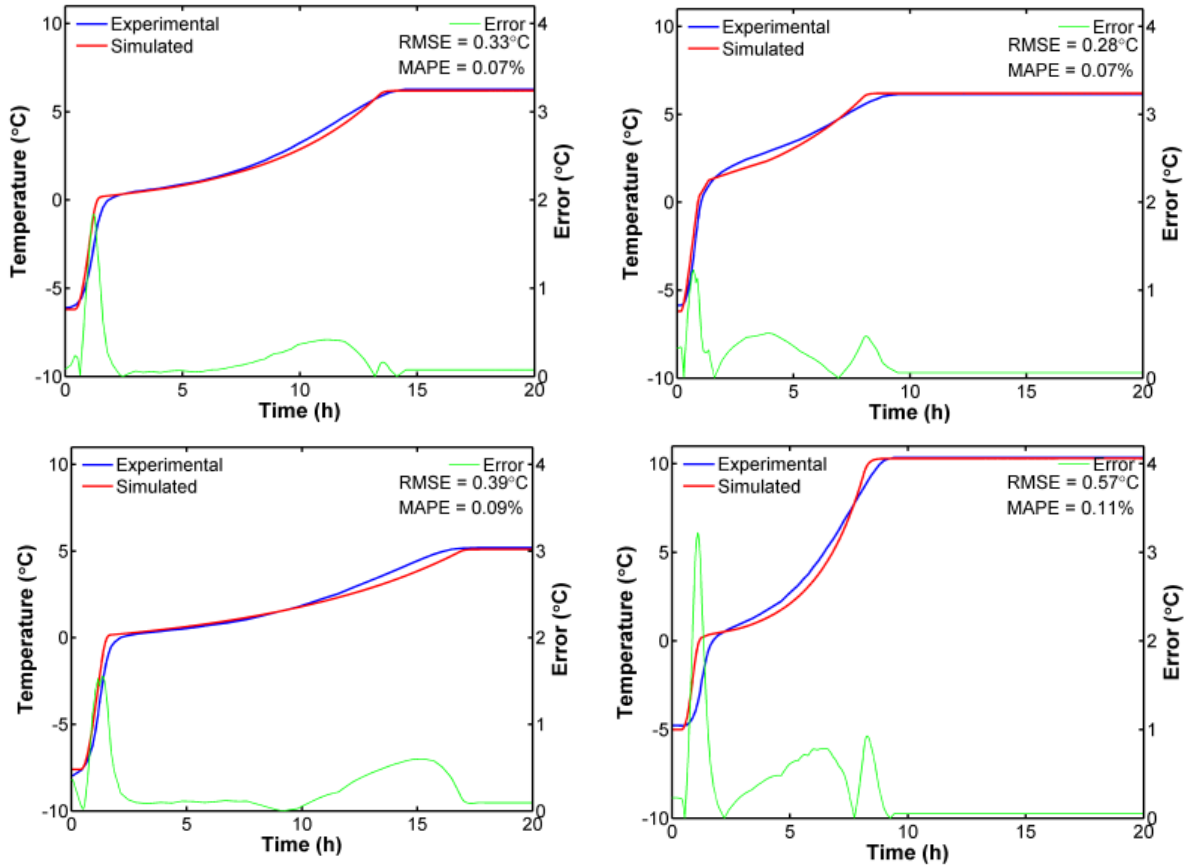

Figure 7: PCM tank thermal discharging validation for (clockwise from top-left) Experiments 10, 13, 14 and 16. Experimental data from Bédécarrats et al. [19].

However, the simulated results still show a strong correlation with the experimental results. The developed TRNSYS model of a PCM TES tank has been shown to accurately predict the outlet HTF temperature from a PCM tank for a range of inlet temperatures and flow rates with acceptable errors [40].

4. Geocooling Simulations

This section uses computer simulation within the TRNSYS environment to analyse the performance of a geocooling system for a small, lightweight office building located in a Mediterranean climate. The integration of a PCM TES tank with the geocooling system is also examined. For comparison, the performance of a GSHP system with no geocooling is used as a reference case. All three systems are evaluated over a four-month cooling season.

Three HVAC systems were simulated and their cooling performance evaluated:

- System 1: Ground-Source Heat Pump cooling with *no* geocooling (reference system),
- System 2: Geocooling,

- System 3: Geocooling with PCM TES.

4.1. Building Model

The simulation building is based on a real building in Septèmes-les-Vallons, situated in proximity to the Mediterranean Sea near Marseilles, France. It is a multi-use, single-story building with an office floor area of 250 m^2 and a workshop area of 88 m^2. The building model was created using the TRNSYS plugin for Google SketchUp (Figure 8). The building is split into 12 conditioned zones with cooling provided by fan coil units (FCUs) (Figure 9). The plant room contains the heat pump, PCM TES tank, and AHU. The building was assumed to be fully occupied with internal loads of 40 W/m^2 between 9am and 6pm, leading to a seasonal average cooling load of 85 kWh per day. Weather data from the TMY2 weather file for Marseille, France, was used in the simulation [41]. For validation purposes, heating and cooling simulations were performed. Heating and cooling loads were calculated zone-by-zone on an hourly basis and then compared with experimental data. Due to space considerations, the building model validation results are not shown in this paper, but can be found in McKenna & Finn, 2013 [2] and McKenna 2015 [1].

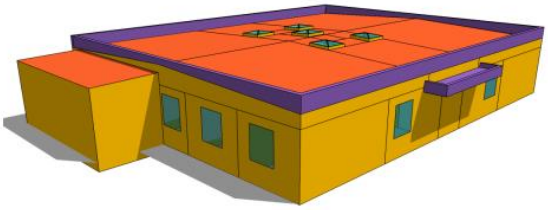

Figure 8: Building model created in TRNSYS using Google SketchUp.

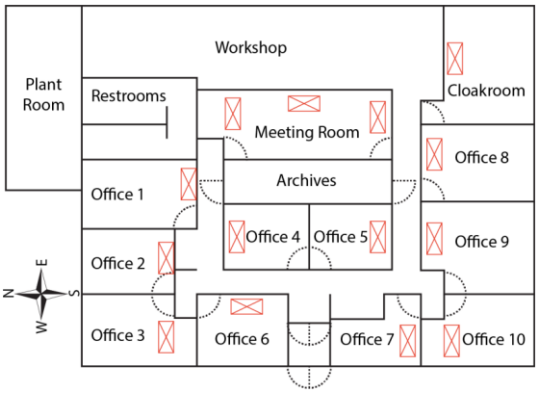

Figure 9: Plan view of the building modelled with FCU locations (red crossed boxes).

4.2. HVAC Systems

The three simulated HVAC systems are described in the following sections, with common attributes described below. For each system, the building is cooled between 8.30 am and 6.30 pm using fan coil units (FCUs) located in the conditioned zones (see Figure 9). The FCUs operate to a cooling set point of 24°C and are supplied by the AHU delivering an airflow rate of 600 kg/h (1 ACH). A four-month cooling season was simulated from the start of June until the end of September. The simulations were run with a time step of one second in order to fully capture system transient behaviour.

Within all three HVAC systems, the primary cooling source is a borehole heat exchanger, consisting of six double U-tube vertical boreholes extending to a depth of 100 m. The HTF used within all three systems is water. A 200 l buffer tank is located on the supply line between the main HP (System 1) or geocooling bypass (Systems 2 and 3) and the air handler unit (AHU) to increase the total thermal mass/capacitance of the HTF. After the buffer tank is a 4.8 l decoupling tank, located across the supply and return lines, which provides hydraulic independence to the primary and the secondary hydronic circuits. Decoupling these loops means that there can be a constant flow rate through the main HP or geocooling bypass, and a varying flow rate through the FCU loop according to the load in the individual zones.

System 1: Ground-Source Heat Pump (GSHP) [Reference System]

The reference system cools the building using a 26 kW GSHP ('Main HP') connected to the borehole heat exchanger. (See McKenna 2015 [1] for a discussion on the development and validation of the heat pump model). A schematic of System 1 can be seen in Figure 10, with the components not considered for this system shown with a lower visual opacity. The main heat pump is cycled to maintain a water supply temperature to the FCUs of 10±1°C. The ground pump (P_1) cycles with the heat pump and provides a ground flow rate of 4.6 m^3/h when the heat pump is on. P_3 is set at a constant 4.6 m^3/h, and P_6 is set to constant pressure control and modulates the water flow to maintain a constant pressure drop across the FCUs. FCU fan speed was set constant at 205 m^3/h.

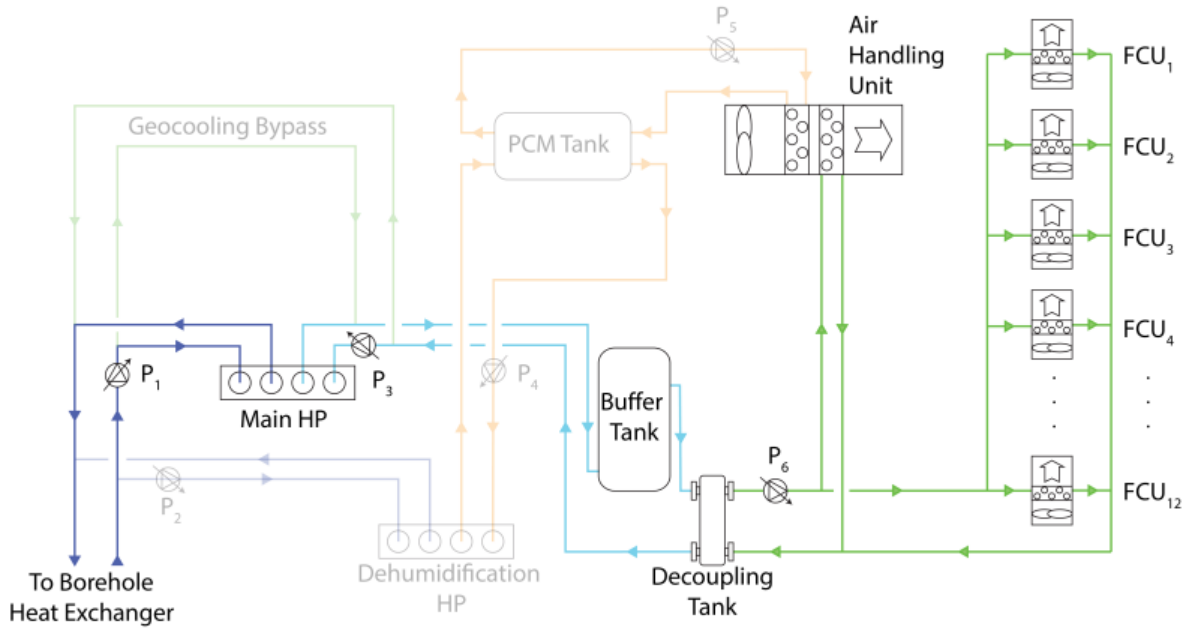

Figure 10: HVAC circuit schematic for System 1 - GSHP.

System 2: Geocooling

For System 2, the main HP is bypassed using a geocooling loop to provide 'free cooling', as shown in Figure 11. The P_1 pump is set to maintain a constant ground water flow rate at 4.6 m^3/h while the flow rate to the building circuit is modulated based on the cooling load. The fan speed of the FCUs was allowed to vary between low (205 m^3/h), medium and high (855 m^3/h) depending on the building cooling load. Increasing fan speeds leads to higher airflow rates but also the generation of more noise and higher energy consumption.

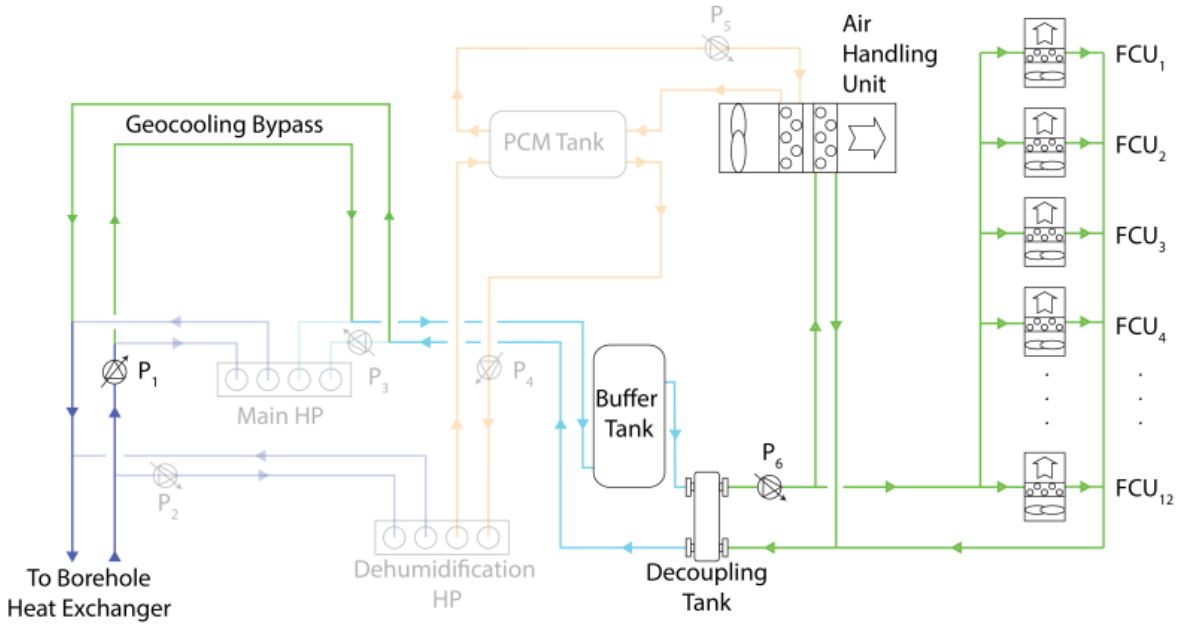

Figure 11: HVAC circuit schematic for System 2 – Geocooling.

System 3: Geocooling with PCM TES

System 3 introduces the PCM TES tank into the System 2 HVAC circuit (see Figure 12). The PCM is charged (i.e., cooled) using a 4.2 kW dehumidification HP, and then discharged via the AHU. The PCM TES tank contains spherically-encapsulated PCM with a melting temperature of 0°C. As with System 2, FCU fan speed was allowed to vary.

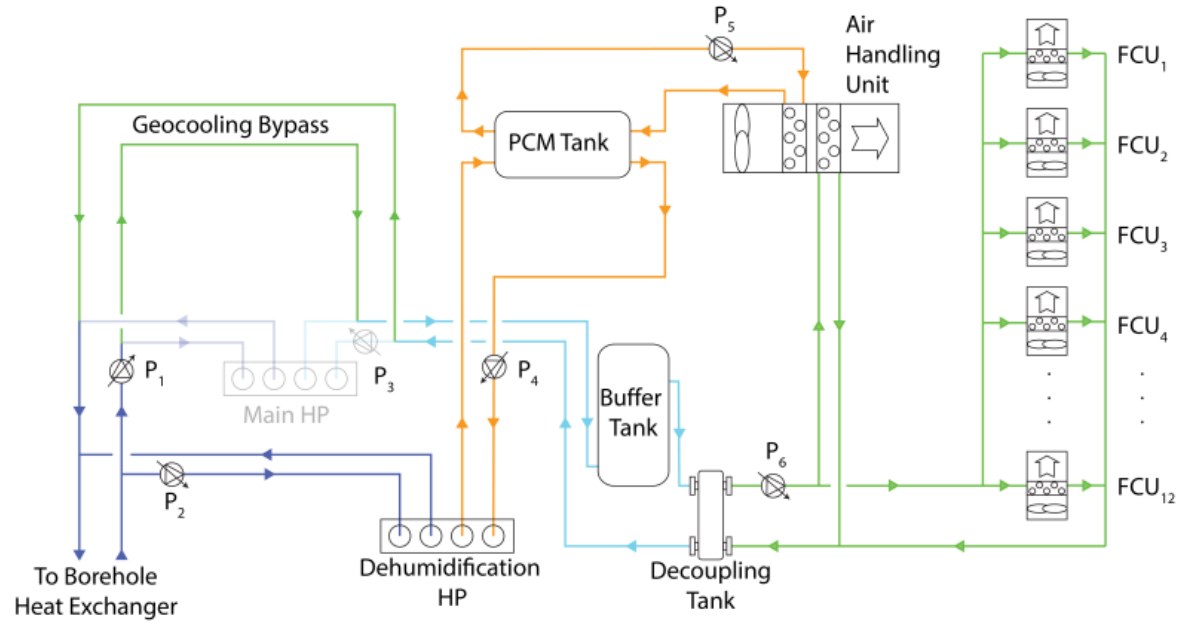

Figure 12: HVAC circuit schematic for System 3 – Geocooling with PCM TES.

Operation of the PCM TES tank was investigated using four scenarios to account for different control strategies, ranging from 'basic' performance (Control Strategy 1) to 'optimal' performance (Control Strategy 4).

The four TES control strategies are:

1. Basic control, i.e., TES tank fully charged each night;
2. Temperature-based control, using ambient temperature forecasts;
3. Load-based control, using ambient temperature and building load forecasts;
4. Optimal control, using perfect foresight of cooling loads.

Control Strategy 1 is the most basic TES control strategy. The TES tank is fully charged at night at then discharged the next day. This strategy can be regarded as the most inefficient because it does not account for cooling loads offset by geocooling. However, Control Strategy 1 is also a simple strategy to implement in real-world applications.

Control Strategy 2 utilises day-ahead weather forecasts to decide if the TES tank should be charged. If the predicted maximum dry-bulb air temperature for the next day exceeds 26°C, then the TES tank is charged overnight.

Control Strategy 3 represents advanced control whereby a simulation model of the building might be used in conjunction with detailed weather forecasts. Next-day building cooling loads are predicted and then used to decide whether the TES tank should be charged or not. If the predicted cooling load exceeds 82 kWh then the TES tank is charged overnight.

Control Strategy 4 describes optimal TES operation, where the TES tank is only used on days where geocooling will not meet 100% of the building cooling loads. As the TES tank must be charged the night before, this strategy relies on perfect foresight of cooling loads and so would not be implementable in practice. However, Control Strategy 4 demonstrates the theoretical limit of TES performance and so serves as a benchmark against which the other three strategies may be judged.

4.3. Seasonal Performance Factor (SPF)

The system seasonal performance factor (SPF) is the main metric by which the performance of the three HVAC systems is evaluated. The SPF of a system (usually a heat pump) is defined as the ratio of the useful thermal energy provided by the system to the electricity consumption of the system over a certain period of time. Under steady-state conditions, the SPF is equivalent to the coefficient of performance (COP):

$$COP = \frac{Q}{W} \qquad Eq.21$$

Where, Q is the useful heating or cooling provided by the system, and W is the work done by the system. Within the context of the three HVAC systems, there are four different SPFs to be considered (Figure 13).

SPF_1 is the useful heat output from the heat pump over a period of time, *t*, divided by the electrical power consumed by the heat pump (Equation 22). SPF_2 includes the power consumed by the pump on the ground loop as part of the denominator (Equation 23). SPF_3 includes the power consumed by the building pump, as well as adding this power to the heat output from the heat pump (Equation 24); it is assumed that all of the electrical energy consumed by the pumps is converted to heat in the HTF, which is added while in heating mode and subtracted while in cooling mode. For SPF_4, the power consumption of the FCUs are included (Equation 25).

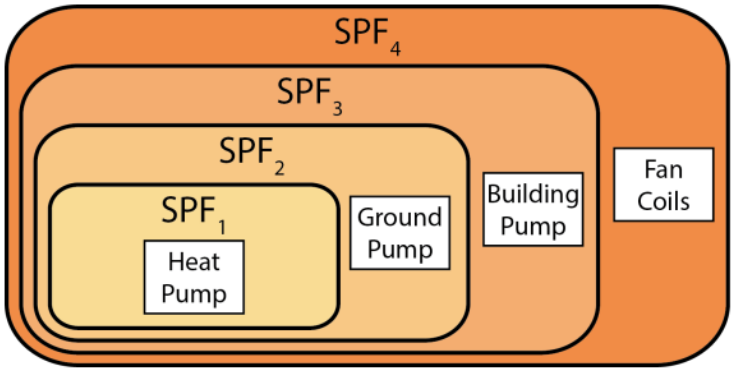

Figure 13: System performance factors. SPF_4 (total system performance) includes SPF_3, SPF_2 and SPF_1.

$$SPF_1 = \frac{\int_0^t Q_{HP}dt}{\int_0^t W_{HP}dt} \qquad Eq.22$$

$$SPF_2 = \frac{\int_0^t Q_{HP}dt}{\int_0^t [W_{HP} + W_{GP}]dt} \qquad Eq.23$$

$$SPF_3 = \frac{\int_0^t [Q_{HP} \pm P_{BP}]dt}{\int_0^t [W_{HP} + W_{GP} + W_{BP}]dt} \qquad Eq.24$$

$$SPF_4 = \frac{\int_0^t [Q_{HP} \pm P_{BP}]dt}{\int_0^t [W_{HP} + W_{GP} + W_{BP} + W_{FC}]dt} \qquad Eq.25$$

Where the subscripts denote heat pump (HP), ground pump (GP), building pump (BP) and fan coil (FC). For each of the three HVAC systems described above, daily and four-month SPFs were evaluated over the cooling season. For electricity price calculations, an off-peak electricity price ratio of 0.6 was assumed.

5. Results and Discussion

Results for the three HVAC system case studies are presented and discussed below.

System 1: GSHP Cooling

Figure 14 shows the daily SPFs plotted for the four-month cooling period (June to September) for System 1 (GSHP with no geocooling). 100% of the building cooling load is met across the entire simulated cooling season.

Due to the relatively low ground temperature, the SPF_1 is very high, with an average value over the season of 8.0. The power consumption of the pumps is quite low, leading to high SPF_2 and SPF_3 values. As the building pump is always on, the value for SPF_3 varies more than SPF_2. This is because the power consumption of the building pump varies little with load. On days with low cooling load, a higher proportion of the cooling energy supplied and the electrical power consumed is attributed to the building pump, compared to days with a higher cooling load. The same is also true for the FCU and AHU power consumption, which leads to the large range of values of SPF_4, varying between 2.5 and 4.0, with an average of 3.5.

The values for SPF_1 and SPF_2 can be seen to decrease over the course of the simulation period. This is due to the ground heating up over the season as heat is rejected to the ground from the building via the borehole heat exchanger. Over the course of the season the ground temperature increases by approximately 1°C.

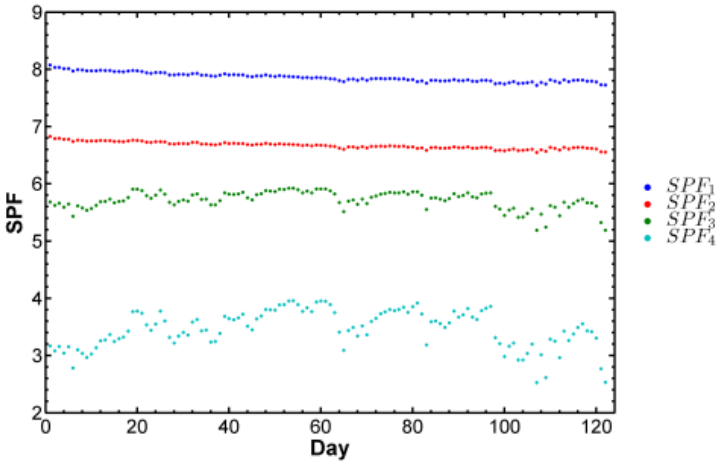

Figure 14: Daily seasonal performance factors (SPFs) for System 1 (GSHP) between June and September.

System 2: Geocooling

Figure 15 shows the daily SPF_3 and SPF_4 for System 2 (Geocooling). Note that SPF_1 and SPF_2 are zero because the main heat pump is not used in System 2. Geocooling alone, with no GSHP, was able to meet the cooling load of the fully-occupied building for 84% of the occupied hours. For 180 hours (out of a total of 1098 occupied hours), spread over 40 separate days, geocooling alone was insufficient and supplementary cooling would be required.

The average SPF_4 over the season is 5.8 compared with 3.5 for System 1. The higher SPFs are due to the reduced electricity consumption from not running the main GSHP in System 1. However, the cooling load delivered by System 2 is less than System 1, so strictly the level of occupant thermal comfort is not directly comparable.

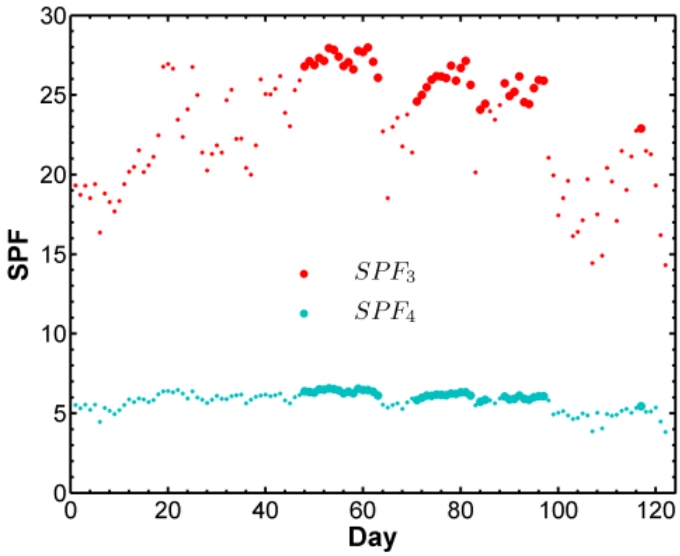

Figure 15: Daily SPF_3 and SPF_4 for System 2 (Geocooling). The larger data points indicate the days when geocooling alone was insufficient to meet the building cooling load.

System 3: Geocooling with PCM TES

Figure 16 shows the daily SPF_4 values for System 3 (Geocooling with PCM TES). For comparison, the SPF_4 values for System 2 are also shown. The SPF4 values for System 3 are less than System 2 due to the additional energy requirement from charging and discharging the PCM TES tank.

By including thermal energy storage, geocooling can meet the building cooling load for 99.6% of the occupied hours. The total cooling load is not met for only four hours across five days. During the hours that the cooling load was not met, the geocooling/TES contribution was only insufficient by 10%, or 1 kW of the total demand. This small shortfall suggests that the occupant discomfort for the four hours would be minimal. The maximum indoor air temperature over this period was 26.3ºC, which is high compared with the 24.0ºC set point, but likely bearable for occupants over a short time duration.

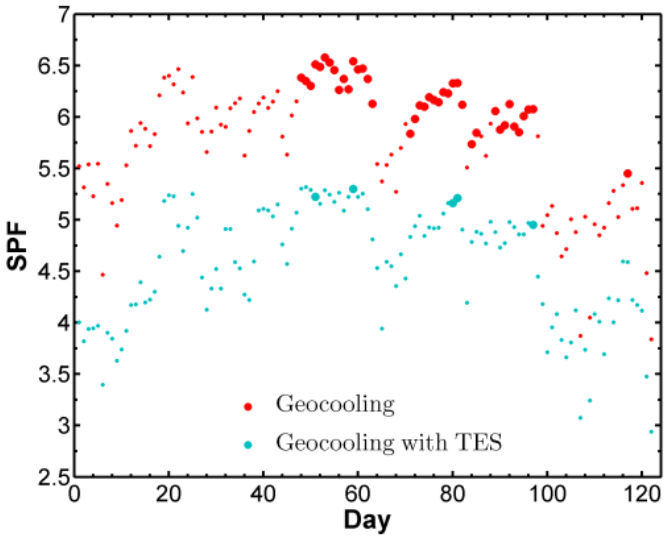

Figure 16: Daily SPF_4 for System 2 (Geocooling) and System 3 (Geocooling with PCM TES).

Table 3 shows the performance of the four TES control strategies with respect to System 1 performance for the four-month period. SPF_4, electricity savings and monetary savings all increase with the sophistication of the control strategy. Control Strategy 4 should be considered the upper limit and not possible to implement practically. However, 24% electricity savings over System 1 (GSHP), using the most crude TES control strategy, for a single cooling season is considerable. 30% electricity savings seen using Control Strategies 2 and 3 should be obtainable with the implementation of an advanced TES control system.

Table 3: Average SPF_4 and savings from System 3 (Geocooling with PCM TES) for the four different TES control strategies. The electricity and monetary savings are calculated with respect to System 1 performance (GSHP).

TES Control Strategy	SPF_4	Electricity Savings (%)	Monetary Savings (%)
1. Basic control	4.6	24	35
2. Temp-based control	5.1	31	38
3. Load-based control	5.1	32	39
4. Ideal control	5.3	34	39

Further electricity savings can be made by varying the water flow rate through the system. Optimal system performance occurs when the water flow rate through the borehole heat exchanger is set equal to the flow rate through the building loop. When this occurs the electricity savings increase to 36, 42, 42 and 45% for Control Strategies 1 to 4, respectively. See McKenna 2015 [1] for more details.

6. Conclusions

This paper has used computer simulation to explore the potential for using geocooling and thermal energy storage (TES) to reduce the energy and carbon impact of cooling a small, lightweight commercial building located in a Mediterranean climate. A new, advanced model for a phase change material (PCM) thermal energy storage (TES) tank was developed and validated.

Geocooling alone was able to meet the cooling loads of the test case building for 84% of a four-month cooling season. The seasonal performance factor (SPF) of the geocooling system was 5.8 compared with 3.5 for a system using a ground-source heat pump (GSHP) with no geocooling. The higher SPF means that the geocooling system was more energy efficient. When geocooling was used in conjunction with TES, the resultant HVAC system was able to meet over 99% of the building cooling loads for the same period.

The work performed in this study indicates geocooling and TES can lead to energy and carbon emission savings for small commercial buildings in Mediterranean climates.

7. Acknowledgements

This research was supported by the European Commission FP7 Programme (TREN/FP7EN/218895/ GROUNDMED). The authors would like to acknowledge the support of project partner CIAT SA, Culoz, France, in particular Mr. Eric Auzenet. William Turner is supported by the Science Foundation Ireland Strategic Partnership Programme (SFI/15/SPP/E3125) and the UCD Energy21 program, co-financed through the Marie Skłodowska-Curie FP7-PEOPLE-2013-COFUND program.

8. Appendix

Table A1: Comparison of the PCM tank used for validation [19] with the modelled PCM tank.

Property	Modelled Tank	Validation Tank
Volume (m^3)	0.5	1.0
Diameter (m)	0.80	0.95
Length (m)	1.00	1.42
Capsule Diameter (mm)	98	77
Capsule Thickness (mm)	1	2
PCM Melting Temperature (°C)	0	0
HTF Flow Rate Charging (m^3/h)	1.5	1.1 to 2.5
HTF Flow Rate Discharging (m^3/h)	0.9	1.0 to 2.3
HTF Inlet Temperature Charging (°C)	-9.0	-3.8 to -6.1
HTF Inlet Temperature Discharging (°C)	-	5.1 to 10.3

9. References

[1] P. McKenna, Cooling solutions for ground source heat pump systems with phase change material thermal energy storage. PhD Thesis, University College Dublin (UCD), 2015.

[2] P. McKenna, D. Finn, A TRNSYS model of a building HVAC system with GSHP and PCM thermal energy storage - Component modelling and validation, in: 13th Conf. Int. Build. Perform. Simul. Assoc., IBPSA, Chambéry, France, 2013: pp. 3336–3343. http://www.ibpsa.org/proceedings/bs2013/p_2349.pdf.

[3] L. Pérez-Lombard, J. Ortiz, C. Pout, A review on buildings energy consumption information, Energy Build. 40 (2008) 394–398. doi:10.1016/j.enbuild.2007.03.007.

[4] IEA, Energy statistics of OECD countries, 2013.

[5] K. Roth, D. Westphalen, J. Dieckmann, S. Hamilton, W. Goetzler, Energy consumption characteristics of commercial building HVAC systems, Volume III: Energy savings potential, 2002.

[6] U. Eicker, Low Energy Cooling for Sustainable Buildings, 2009. ISBN: 047069744X.

[7] D. Pahud, M. Belliardi, P. Caputo, Geocooling potential of borehole heat exchangers' systems applied to low energy office buildings, Renew. Energy. 45 (2012) 197–204. doi:10.1016/j.renene.2012.03.008.

[8] D. Christantoni, S. Oxizidis, D. Flynn, D.P. Finn, Implementation of demand response strategies in a multi-purpose commercial building using a whole-building simulation model approach, Energy Build. 131 (2016) 76–86. doi:10.1016/j.enbuild.2016.09.017.

[9] B. Price, Maintenance for energy efficiency and ongoing hvac system tuning, in: Aust. Inst. Refrig. Air Cond. Heat. Pre-Loved Build. - Sustain. Exist. Build. Stock, Melbourne, Australia, 2006: pp. 1–18.

[10] U. Eicker, C. Vorschulze, Potential of geothermal heat exchangers for office building climatisation, Renew. Energy. 34 (2009) 1126–1133. doi:10.1016/j.renene.2008.06.019.

[11] W. Wu, T. You, B. Wang, W. Shi, X. Li, Evaluation of ground source absorption heat pumps combined with borehole free cooling, Energy Convers. Manag. 79 (2014) 334–

343. doi:10.1016/j.enconman.2013.11.045.

[12] J. Lund, B. Sanner, L. Rybach, R. Curtis, G. Hellstrom, Geothermal (Ground Source) Heat Pumps, A World Overview, Oregon Institute of Technology, Oregon, 2004.

[13] B. Sanner, C. Karytsas, D. Mendrinos, L. Rybach, Current status of ground source heat pumps and underground thermal energy storage in Europe, Geothermics. 32 (2003) 579–588. doi:10.1016/S0375-6505(03)00060-9.

[14] P. Denholm, M. Hand, Grid flexibility and storage required to achieve very high penetration of variable renewable electricity, Energy Policy. 39 (2011) 1817–1830. doi:10.1016/j.enpol.2011.01.019.

[15] US DOE, Grid energy storage, 2013. https://energy.gov/sites/prod/files/2014/09/f18/Grid Energy Storage December 2013.pdf.

[16] IEA, Technology roadmap - energy storage, 2014. http://www.iea.org/publications/freepublications/publication/technologyroadmapenergystorage.pdf.

[17] IEA-ETSAP, IRENA, Thermal energy storage. Technology Brief E17., 2013. https://www.irena.org/DocumentDownloads/Publications/IRENA-ETSAP Tech Brief E17 Thermal Energy Storage.pdf.

[18] J.E. Braun, Reducing Energy Costs and Peak Electrical Demand Through Optimal Control of Building Thermal Storage, ASHRAE Trans. 96 (1990) 876–888.

[19] J.P. Bédécarrats, J. Castaing-Lasvignottes, F. Strub, J.P. Dumas, Study of a phase change energy storage using spherical capsules. Part II: Numerical modelling, Energy Convers. Manag. 50 (2009) 2537–2546. doi:10.1016/j.enconman.2009.06.003.

[20] J. Bony, S. Citherlet, Numerical model and experimental validation of heat storage with phase change materials, Energy Build. 39 (2007) 1065–1072. doi:10.1016/j.enbuild.2006.10.017.

[21] S.L. Chen, One-Dimensional Analysis of Energy Storage in Packed Capsules, J. Sol. Energy Eng. 114 (1992) 127. doi:10.1115/1.2929992.

[22] Y. Dutil, D.R. Rousse, N. Ben Salah, S. Lassue, L. Zalewski, A review on phase-change materials: Mathematical modeling and simulations, Renew. Sustain. Energy Rev. 15 (2011) 112–130. doi:10.1016/j.rser.2010.06.011.

[23] A. Felix Regin, S.C. Solanki, J.S. Saini, An analysis of a packed bed latent heat thermal energy storage system using PCM capsules: Numerical investigation, Renew. Energy. 34 (2009) 1765–1773. doi:10.1016/j.renene.2008.12.012.

[24] M. Ibáñez, L.F. Cabeza, C. Solé, J. Roca, M. Nogués, Modelization of a water tank including a PCM module, Appl. Therm. Eng. 26 (2006) 1328–1333. doi:10.1016/j.applthermaleng.2005.10.022.

[25] A.T. Jones, D.P. Finn, Co-simulation of a HVAC system-integrated phase change material thermal storage unit, J. Build. Perform. Simul. 10 (2017) 313–325. doi:10.1080/19401493.2016.1257068.

[26] G. Henze, R. Dodier, M. Krarti, Development of a Predictive Optimal Controller for

Thermal Energy Storage Systems, HVAC&R Res. 3 (1997) 233–264. doi:10.1080/10789669.1997.10391376.

[27] G. Henze, C. Felsmann, G. Knabe, Evaluation of optimal control for active and passive building thermal storage, Int. J. Therm. Sci. 43 (2004) 173–183. doi:10.1016/j.ijthermalsci.2003.06.001.

[28] M. Kintner-Meyer, A.F. Emery, Optimal control of an HVAC system using cold storage and building thermal capacitance, Energy Build. 23 (1995) 19–31. doi:10.1016/0378-7788(95)00917-M.

[29] J.E. Braun, Impact of control on operating costs for cool storage systems with dynamic electric rates, in: ASHRAE Trans., 2007: pp. 343–354.

[30] J. Wei, Y. Kawaguchi, S. Hirano, H. Takeuchi, Study on a PCM heat storage system for rapid heat supply, Appl. Therm. Eng. 25 (2005) 2903–2920. doi:10.1016/j.applthermaleng.2005.02.014.

[31] S. Bellan, J. Gonzalez-Aguilar, A.R. Archibold, M. Romero, M.M. Rahman, D.Y. Goswami, et al., Transient numerical analysis of storage tanks based on encapsulated PCMs for heat storage in concentrating solar power plants, Energy Procedia. 57 (2014) 672–681. doi:10.1016/j.egypro.2014.10.222.

[32] C. Kendrick, N. Walliman, Removing Unwanted Heat in Lightweight Buildings Using Phase Change Materials in Building Components: Simulation Modelling for PCM Plasterboard, Archit. Sci. Rev. 50 (2007) 265–273. doi:10.3763/asre.2007.5032.

[33] G.R. Solomon, S. Karthikeyan, R. Velraj, Sub cooling of PCM due to various effects during solidification in a vertical concentric tube thermal storage unit, Appl. Therm. Eng. 52 (2013) 505–511. doi:10.1016/j.applthermaleng.2012.12.030.

[34] D.Y. Goswami, Principles of Solar Engineering, Third Edition, 2015. doi:10.1017/CBO9781107415324.004.

[35] T.E.W. Schumann, Heat transfer: A liquid flowing through a porous prism, J. Franklin Inst. 208 (1929) 405–416. doi:10.1016/S0016-0032(29)91186-8.

[36] V. Alexiades, A.D. Solomon, Mathematical modeling of melting and freezing processes, J. Fluid Mech. 251 (1993) 336. doi:10.1017/S0022112093213593.

[37] G. Nellis, S. Klein, Heat Transfer, 2009. ISBN: 0521881072.

[38] H. Mehling, L.F. Cabeza, Heat and cold storage with PCM, Springer Berlin Heidelberg, Berlin, Heidelberg, 2008. doi:10.1007/978-3-540-68557-9.

[39] S.A. Klein, TRNSYS 17: A Transient System Simulation Program, (2010). http://sel.me.wisc.edu/trnsys.

[40] ANSI/ASHRAE, ASHRAE Guideline 14-2002 Measurement of Energy and Demand Savings, ASHRAE. 8400 (2002) 170.

[41] NREL, TMY2 Weather Files, (1995). http://rredc.nrel.gov/solar/old_data/nsrdb/1961-1990/tmy2/.